Available online at www.sciencedirect.com
ScienceDirect
Ocean Modelling 17 (2007) 219–238
Ocean Modelling
www.elsevier.com/locate/ocemod

Empirical and stochastic formulations of western boundary conditions

T. Mike Chin *, Tamay M. Özgökmen, Arthur J. Mariano

Rosenstiel School of Marine and Atmospheric Science, University of Miami, Miami, FL 33149, United States

Received 17 July 2006; received in revised form 12 February 2007; accepted 12 February 2007
Available online 24 February 2007

Abstract

High-frequency radar observations of surface current at 100 m resolution are used to stochastically determine the vorticity variability in the boundary layer between the Florida Current and the Florida coast. Using the empirical data, several formulations of the stochastic boundary condition (SBC) are then developed and evaluated for the parameterization of sub-grid scale variability along the western boundaries of an ocean general circulation model (OGCM). These SBCs are compared to both no-slip and free-slip boundary conditions along the western boundary of a channel model simulating separation of the boundary current at a cape, as well as simulations of the classic, wind-forced double-gyre circulation. Our studies indicate that simulated circulation patterns are sensitive to both the functional form of the SBC and the parameters used in a given formulation. In particular, a relatively simple, auto-regressive formulation of SBC can be applied to a coarse-resolution, eddy-permitting OGCM to increase flow turbulence and to affect the flow patterns in ways distinct from the standard, deterministic no-slip and free-slip boundary conditions. Correlation time scales of a few days to weeks, orders of magnitude larger than a typical time step of OGCM, are needed in the regression model for SBC. This formulation of SBC is shown to be effective in both quasi-geostrophic and shallow-water dynamics.

1. Introduction

The western boundary currents and associated circulation patterns downstream from them are some of the most prominent and energetic features in the ocean and climate systems. Adequate representation of such currents like the Gulf Stream is indeed crucial for numerical simulation of global energy and heat transports (Treguier, 1992; Beckman et al., 1994; Böning et al., 1994). In particular, the boundary layer between the current and coast is rich in turbulent activities, including "spin-off eddies" that can persist up to 3 weeks and advect along the coast (Lee, 1975; Lee et al., 1981; Lee and Atkinson, 1983), which are too small to be resolved by global-scale ocean general circulation models (OGCMs) with a typical grid-spacing of O(10) km or larger. Gross effects of the boundary-layer processes are usually lumped into one of the traditional boundary

* Corresponding author. Address: RSMAS/MPO, 4600 Rickenbacker Causeway, Miami, FL 33149, United States. Tel.: +1 818 393 2510.
E-mail address: tchin@rsmas.miami.edu (T.M. Chin).

1463-5003/$ - see front matter © 2007 Elsevier Ltd. All rights reserved.
doi:10.1016/j.ocemod.2007.02.001

conditions based on zero tangential velocity (*no-slip*) and zero stress (*free-slip*). A linear combination of these two types of boundary conditions (*partial slip*) has also been proposed (Haidvogel et al., 1991). These boundary conditions can lead to substantially different model behavior not only in the western boundary currents (e.g. Özgökmen et al., 1997) but also in the basin-wide circulation (e.g. Böning, 1986). However, variability within the boundary layer is completely lost since the traditional formulations are invariant both in space and time. To account for such variability, we consider here stochastic formulations for the boundary condition.

Both eddy viscosity and grid spacing have strong impacts on the dynamics of western boundary currents. It can be shown by dimensional arguments that the eddy viscosity ν scales as a function of the grid spacing Δ as $\nu \sim \epsilon\Delta$, where ϵ is the sub-grid scale turbulent fluctuation velocity. For typical values of $\epsilon = O(10^{-2})$ m/s and $\Delta = 10^5$ m in climate models, the viscosity is $\nu = O(10^3)$ m^2/s, which is much more viscous than actual ocean where $\nu = O(10^{-6})$ m^2/s. It is known from classical fluid dynamics that the width of the viscous shear layer near solid boundaries is a stronger function of the Reynolds number Re than the scales of turbulent motion in the interior flow (Schlichting, 1979). Using typical values of current speed $U \approx 1$ m/s and boundary layer width $L \approx 10^5$ m of the Florida Current, we have $Re = UL/\nu \approx 10^{11}$, while climate models could only achieve $Re \approx 10^2$. Thus, the width of the shear layer and hence the stress exerted by the wall into the fluid interior are drastically under-valued. Note that a much lower value of ν cannot simply be used in climate models since large grid spacing leads to a resolution error, which will eventually cause numerical instability. Clearly, the use of no-slip boundary condition would not supply appropriate amount of wall stress in a typical OGCM whose viscous boundary layer is under-resolved, while the free-slip formulation ignores such stress altogether.

Climate scale ocean model usually do not have resolution for the typically narrow boundary currents. An obvious remedy is to decrease the grid spacing near the boundaries, so that both the resolution error arising from projecting the dynamics onto a coarse grid as well as the ambiguity of the boundary condition can be eliminated. This approach would be impractical in OGCMs based on finite-difference numerical schemes, due to realization issues for variable grid spacing and potential for large increase in computational cost. We thus need to consider an alternate formulation of the western boundary condition that allows more flexible parameterization of the boundary dynamics in terms of the effect that they induce on basin-scale circulation patterns and energetics.

In this paper, we develop empirical models based on observations of the dynamics of the western boundary layer. Recent measurements from the high-frequency (HF) radar instruments yield surface current fields at high enough resolution, in both space and time, that allow direct observations of sub-mesoscale eddy activities along the Florida coast (Shay et al., 2000). These sub-grid scale eddies could potentially serve as reservoirs of potential vorticity that feeds momentum back into the main boundary current. Several formulations of stochastic boundary condition (SBC) are derived to be consistent with these HF observations. We then compare the SBCs in a series of simplified numerical simulations of ocean circulation in terms of their impacts on mesoscale and larger circulation patterns. We examine morphological changes in the western boundary and its downstream currents in response to introduction of random vorticity anomalies in the upstream portion by such SBCs.

Use of random processes to correct for deficiencies in OGCMs due to the limitation in numerical resolution has been an active research topic (e.g., Treguier and Hua, 1987; Griffa and Castellari, 1991; Berloff, 2005). Much of the research focus is on development of processes that can replace the traditional formulations for horizontal diffusion and sub-grid scale turbulence (Berloff, 2005, and references therein), and few has so far examined the lateral boundary conditions in the context of injecting random perturbations to potential vorticity. Our preliminary work (Mariano et al., 2003) has shown that an empirically derived SBC can lead to formation of coherent meso-scale structures and energetics that are significantly different from those obtained with free-slip and no-slip. This preliminary SBC formulation, however, has practical difficulties that limit its application beyond the simple, channel configuration of the QG model (Mariano et al., 2003). A motivation for the study presented here is to address these difficulties to provide a more practical recipe for SBCs and to show that it is applicable to other model configurations including primitive equation models.

Specifically, in the previous work, an advecting spatially regressive process has been used in attempt to capture the prominent features of the HF observation in a single formulation. The random process is generated at a single (up-stream) location on the western boundary, instead of all along the boundary. Such a location

dependency in the stochastic process is obviously artificial. Also, the advection component has posed inherent numerical problems due to difficulty in dealing with the high frequency and wavenumber process as well as with the changes in the advection speeds and directions which are apparently dependent on the ambient mean flow. Finally, in the previous work, the model time step Δt has been matched exactly with the sampling intervals of the HF observation data from which the SBC formulation is derived. The SBCs developed under this work are aimed to relieve these restrictions. Our approach here is to decompose the observed boundary layer behaviors into several dynamical components, to formulate an SBC for each of these components, and to determine impacts of each SBC formulation on the simulated flows.

2. Boundary layer observation

2.1. Observations

Satellite images now allow us to observe that the sub-mesoscale (10–25 km diameter) surface eddies are distributed broadly over the global oceans and are "overwhelmingly cyclonic" (Munk et al., 2000). Sighting of these features depends on surface condition (light wind) as well as on location (no such features within 6° of equator) and time (seasonal, in parts of Mediterranean). One of possible causes for these eddies is shear instability. The smaller cyclonic eddies are often associated with larger anticyclonic features such as the Loop Current and Warm Core Rings.

Smaller eddies of 1–10 km diameters have also been observed with in situ techniques, often in the coastal boundary zones. Coastal eddies have been recorded off California Current (DiGiacomo and Holt, 2001). The "frontal eddies" and "spinoff eddies" are also observed between the Florida Current and the coast and are of particular interest in this paper. Synoptic observations (Lee, 1975; Lee et al., 1981; Lee and Atkinson, 1983) have recorded sub- to near-grid scale eddies that occur aperiodically between the western boundary current and coast, persist up to 3 weeks, and advect along current at speed (25–100 cm/s) which is a significant fraction of the mean current.

The four-dimensional current experiment has provided gridded velocity data for a 28-day period in July/August, 1999 (Shay et al., 2002; Peters et al., 2002), based on Ocean Surface Current Radar (OSCR) measurements (u, v) over a 7 km × 8 km area along the southeastern Florida coastline, at horizontal and temporal resolutions of ~250 m and 15 min, respectively. The measurements are in a region of large ambient relative vorticity, with a Rossby number of O(10), due to the close proximity of the Florida Current on the narrow South Florida Shelf.

2.2. OSCR statistics

Relative vorticity, $\zeta(x, y, t) = \partial v/\partial x - \partial u/\partial y$, is computed from the OSCR velocity measurements and is used as the basis for our formulation of boundary conditions. The time-averaged vorticity field (Fig. 1) indicates that a south-to-north ridge of the maximum vorticity, due mostly to the along-shore shear, bisects the observation domain approximately 5 km off-shore. The width δ_x of this vorticity ridge is approximately 5 km. The vorticity values are positive (cyclonic) with few exception, and the maximum vorticity along each cross-stream (longitudinal) line $\hat{\zeta}(y, t) = \max_x \zeta(x, y, t)$ is studied statistically.

Time series of $\hat{\zeta}(y, t)$ at any fixed y (Fig. 2) displays energetic and episodic nature of the near-shore vorticity, with temporal scales ranging from hours to a week and peak values greater than ten times the ambient Coriolis frequency (~$6.4 \times 10^{-5}\ s^{-1}$). The space–time mean $\hat{\zeta}_m$ of OSCR vorticity $\hat{\zeta}$ is observed to be $3.93 \times 10^{-4}\ s^{-1}$ with a standard deviation of $1.29 \times 10^{-4}\ s^{-1}$. The e-folding scales of the auto-correlation function of $\hat{\zeta}(y, t)$ are approximately 10 km along the latitude y and 2 h along time t. Fig. 3 displays the auto-correlation values as a function of latitudinal and temporal lags $(\Delta y, \Delta t)$. The maximum correlation values are concentrated tightly along a ridge, to which a least-squares fit can be made as indicted by the thick grey line in Fig. 3. This is a strong indication of the nearly constant advection speed to the north, and the slope of the fitted line yields an estimate of the advection speed to be 59.5 cm/s. The correlation field (Fig. 3) also indicates much weaker local maxima at $\Delta t = \pm 10$ h, consistent with the 10-h periodicity in the underlying velocity field (u, v) as reported by Peters et al. (2002) and Shay et al. (2002). The temporal dynamics are dominated by O(1) km-scale

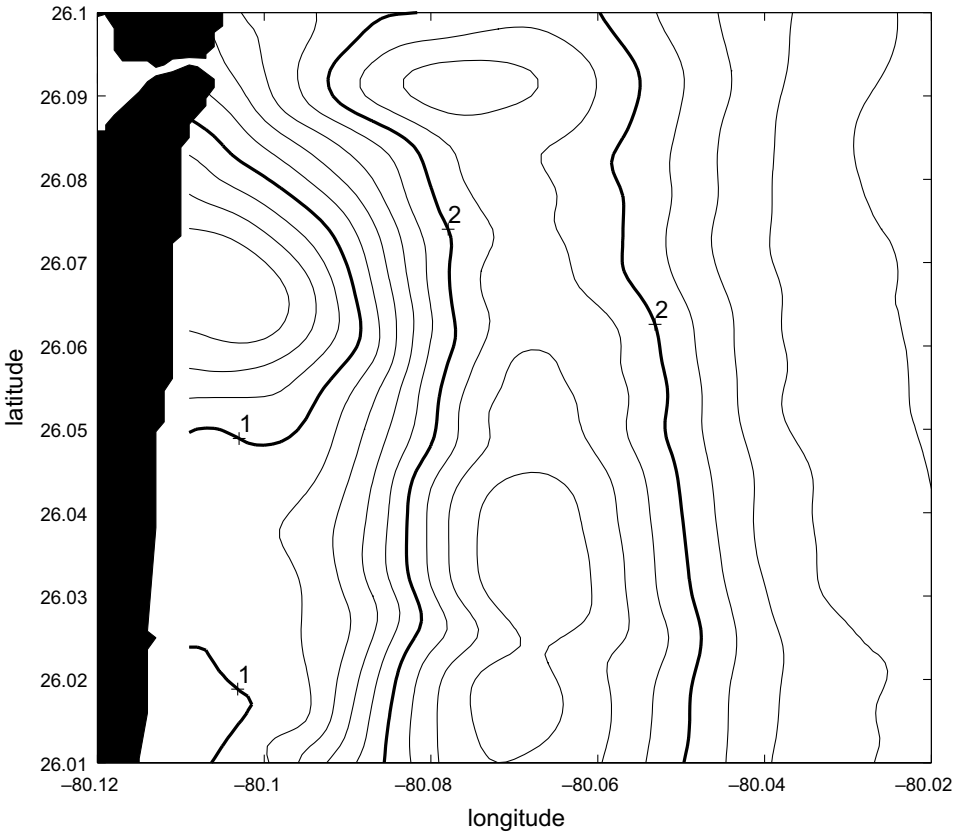

Fig. 1. Mean vorticity field from OSCR velocity data. The unit of contour labels is $1 \times 10^{-4}\ s^{-1}$. Coastline near Fort Lauderdale, Florida is also shown to the left.

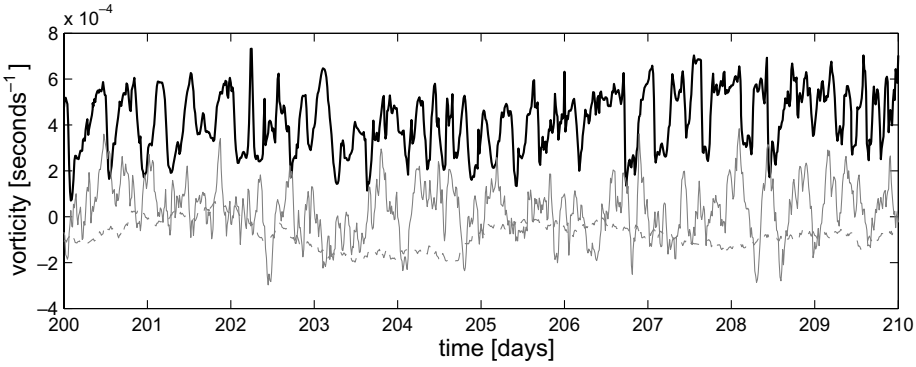

Fig. 2. Vorticity observed from OSCR data ($\hat{\zeta}(y,t)$ for a fixed y, thick solid line) and simulated vorticity time series (from the T0 model, thin solid line; from the T1 model, thin dashed line).

cyclonic vortices, and motion energetic at periods of 10- and 27-h (Peters et al., 2002; Shay et al., 2002), as well as longer temporal scales (Soloviev et al., 2003), have also been observed. The temporal power spectral density (thin line, Fig. 4) shows a peak at the dominant 10-h period (0.1 cph), as well as a power-law of the slope of approximately −2 both on the high- and low-frequency sides of the 10-h peak. The 10-h peak, however, is also observed to be seasonal, occurring mostly during the summer (Soloviev et al., 2003) which coincides with the OSCR data.

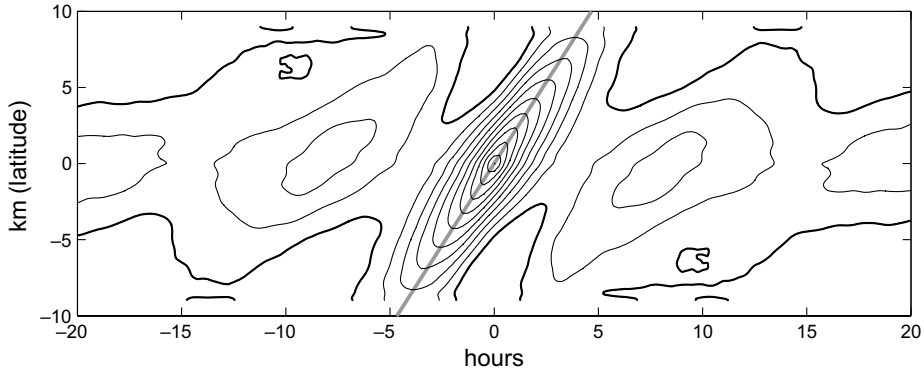

Fig. 3. Space-time auto-correlation field of $\hat{\zeta}(y,t)$ from OSCR data. The thick curves are the zero correlation contours, and the contour interval is 0.1. The light thick straight line across the center is a least-squares fit of a line along the ridge of high correlation values, and its slope indicates an advection speed of approximately 59.5 cm/s.

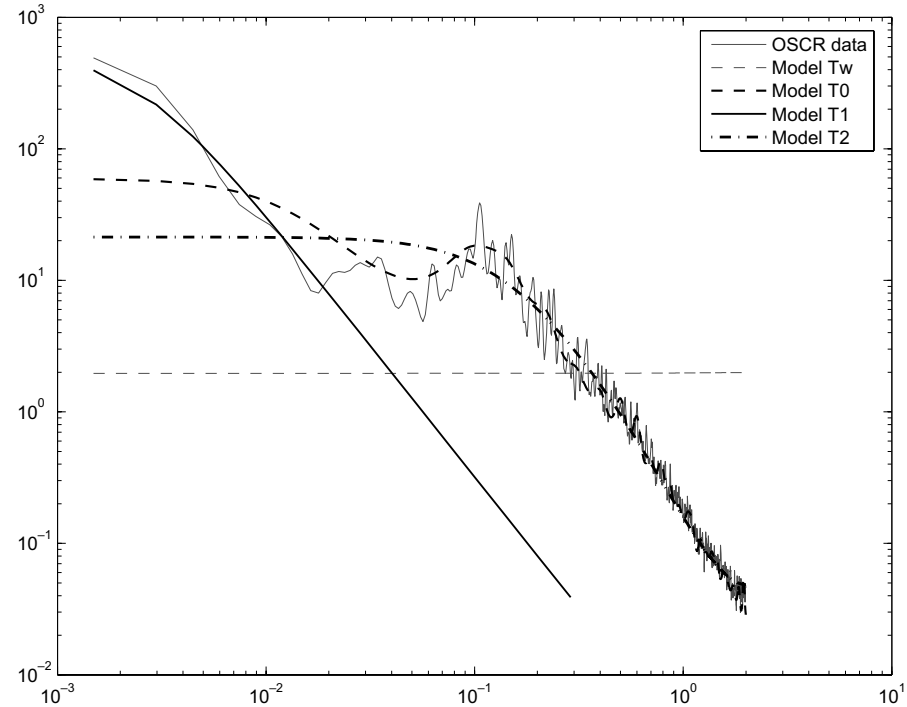

Fig. 4. Power spectral densities of vorticity, as a function of cph (cycles per h), computed from OSCR velocity data (thin solid line) and simulated using the Tw (thin dash), T0 (thick dash), T1 (thick solid), and T2 (dash-dot) models.

3. Stochastic boundary conditions (SBC)

The two prevailing features of the along-shore vorticity $\hat{\zeta}(y,t)$ observed from the OSCR data are (i) the northward advection speed of 59.5 cm/s and (ii) the multi-time-scale dynamics. We model each of these feature statistically. To focus on the space–time variability, our modeling is based on the detrended signal $\tilde{\zeta}(y,t) \equiv \hat{\zeta} - \hat{\zeta}_m$.

3.1. SBC by temporal regression (Type T)

To model the temporal dynamics, we use auto-regression (AR) formulations to fit several prominent characteristics of the empirical spectrum (thin line, Fig. 4). The modeled features are: the total variance (modeled

as a white noise), the 10-h period, and the power-laws near the low- and high-frequency ends. An AR-p model, where p is the order (complexity) of regression, can usually be fit readily to a spectral feature at a given temporal scale, while a fit by single AR model to features over scales that differ by orders of magnitude is more difficult. The four resulting AR models, used in our study, are labeled, respectively, as

"Tw" (white-noise),
"T0" (10-h periodicity),
"T1" (low-frequency component),
"T2" (high-frequency component).

For these models, the grid-to-grid spatial correlation as well as along-shore advection speed are both assumed to be zero. Fig. 4 shows the spectral densities of boundary vorticities simulated using the AR models. For the T0 model, a regression model with a high order (AR-50 for a sampling time interval $\Delta t = 15$ min, while AR-13 and AR-6 for Δt of 1 and 2 h, respectively) is found necessary to capture both the 10-h peak and high-frequency power-law slope. For the T1 model, an AR-1 model is sufficient to fit only the low-frequency slope. Although the slopes of the high- and low-frequency power-laws are similar, an AR-2 model is used for the T2 model to fit the sharp drop-off near the 10-h peak. For a given stochastic process, the regression coefficients vary with the sampling interval Δt, which is 15 min for the OSCR data. The observation $\tilde{\zeta}(y,t)$ can be decimated in time to evaluate the coefficients for integer multiples of the time steps, such as for Δt of 1 and 2 h. The regression coefficient values for $\Delta t = 2$ h are given in Table 1 for the four SBC models.

To fit an AR-1 model to the low-frequency slope, $\tilde{\zeta}(y,t)$ is first low-pass filtered to remove the higher frequency components including the 10-h periodicity; the residual, which is responsible for the -2 power-law slope at the low-frequency end, is then processed using the Yule–Walker procedure to obtain the single regression coefficient. The AR-1 regression coefficient can be expressed in terms of the e-folding time scale τ_1 as $\exp(-2\pi\Delta t/\tau_1)$. For any AR-1 model, the time constant τ_1 and interval-integrated white-noise variance $\sigma^2\Delta t$ are invariant over a range of model time step Δt. Since Δt values are dictated by OGCMs, these values would then be more useful (universal) as the controlling parameters for the T1 stochastic boundary condition model. The empirical values from the OSCR data are $\tau_1 = 6.7 \pm 1.9$ days and $\sigma^2\Delta t = 2.6 \times 10^{-10}\ \mathrm{s}^{-1}$.

3.2. SBC by advecting of white noise (Type A)

To numerically realize the advection, we note that the observed advection speed implies a translation by a sub-grid length over a typical model time step, e.g., a 2.1 km of translation when the time step is 1 h. A locally cubic polynomial (the B-spline) has thus been applied to the randomly generated vorticity values before translation. The specific numerical procedure is as follows: (1) generate a Gaussian white noise sequence along the

Table 1
The square-root variance (σ, in the unit of 1/s) and auto-regression coefficients obtained from the OSCR measurements for each of the stochastic boundary conditions (SBC)

SBC	σ [1/s]	Coefficients
Tw	1.29×10^{-4}	
T0	1.19×10^{-4}	$c_1 = 0.195$ $c_2 = -0.074$ $c_3 = 0.102$ $c_4 = 0.140$ $c_5 = 0.086$ $c_6 = 0.046$
T1	2.32×10^{-5}	$c_1 = 0.988$
T2	1.23×10^{-4}	$c_1 = 0.231$ $c_2 = -0.034$

These values are valid only for time step (Δt) of 2 h.

western boundary grid points using a mean of zero and standard deviation of $1.29 \times 10^{-4}\ \mathrm{s}^{-1}$ corresponding to the space–time variability of the OSCR vorticity; (2) apply spline to the random sequence to approximate a spatially continuous function $z(y)$; (3) translate the function in space based on a given advection speed α to obtain the boundary vorticity $\tilde{\zeta}(y,t) = z(y - \alpha t)$. We refer to this SBC formulation as the "A(α)" model, where α is the advection speed in cm/s. Since the observed speed is $\alpha \approx 0.6$ m/s, the formulation consistent with the OSCR data would be A(60). We have experimented with several other speed values, as detailed later. Note that the A(∞) model is equivalent to the Tw model.

4. Experiments and methods

Numerical simulations of the western boundary current are used to investigate impacts of the boundary-layer variability on the circulation patterns and energetics. We choose the free-slip boundary condition as the control case, since it implies null shear activity at the boundary. Each of the SBC formulations from the previous section as well as a no-slip formulation then replaces the free-slip condition along the western boundary, and the resulting simulations of circulation are compared. The comparison experiments are conducted with three different single-layer circulation models described here.

4.1. The periodic-channel (QG-Cape) experiment

A "periodic channel" model over a rectangular domain, where the north and south boundaries are joined for periodicity in the y-direction and east and west boundaries are solid, is used to simulate a western boundary current using the quasi-geostrophic (QG) dynamics with a prescribed south-to-north transport $T_0 = 30$ Sv, which equals to the average transport of the Florida Current (Leaman et al., 1989). The domain dimension is 3000 km × 2000 km with a 20 km grid spacing.

Following Özgökmen et al. (1997), we placed a lateral obstacle that represents the coastline near Cape Hatteras to simulate the separation of the Gulf Stream from the shore. It is known (as we will also see) that the boundary current tends not to separate from the shore when the free-slip boundary condition is used at the western boundary, while use of a no-slip formulation facilitates separation. The lateral boundary feature, or the "Cape" hereafter, is implemented as an isosceles triangle whose base is 500 km along the western boundary and height is 250 km protruding into the boundary current (see Fig. 5).

The governing equations of the reduced-gravity QG dynamics used here are

$$\frac{\partial q}{\partial t} + aJ(\psi, \nabla^2\psi) + b\frac{\partial \psi}{\partial x} = d\nabla^4\psi + ew_{\mathrm{E}}, \tag{1}$$

$$\nabla^2\psi - \psi = q, \tag{2}$$

where ψ, x, y, t are non-dimentionalized so that $(T_0H^{-1})\psi$, $R_{\mathrm{d}}x$, $R_{\mathrm{d}}y$, and $f_0^{-1}t$ are, respectively, the stream-function, zonal and meridional distances, and time. The key model parameters are given in Table 2, where H is the active layer depth, $R_{\mathrm{d}} = \sqrt{g'H}/f_0$ is the radius of deformation, f_0 and β, respectively, are the mean and the meridional gradient of the Coriolis frequency, g' is the reduced gravity parameter, w_{E} is wind-forced Ekman pumping, and ν is the horizontal viscosity. The non-dimensional coefficients are defined as $a \equiv T_0/(HR_{\mathrm{d}}^2 f_0)$, $b \equiv \beta R_{\mathrm{d}}/f_0$, $d \equiv \nu/(R_{\mathrm{d}}^2 f_0)$, and $e \equiv \beta R_{\mathrm{d}}^2/(f_0 L_x)$. Consult Mariano et al. (2003) and references therein for more details of the dynamics.

The model is configured in a mid-latitude rectangular domain. The meridional length of 3000 km is adequate to contain several wavelengths of characteristic instabilities of the western boundary current. The zonal length of 2000 km is much wider than the meso-scale eddies and the width has negligible impact on the solution. The equilibrium layer thickness ($H = 5000$ m) and the stratification ($g' = 0.01\ \mathrm{m\ s}^{-1}$) are such that the Rossby radius of deformation is 24 km, typical of mid-latitude circulation. The viscosity is taken as $\nu = 400\ \mathrm{m}^2\ \mathrm{s}^{-1}$, which is high enough to ensure numerical stability at the selected grid scale, but also small enough to allow highly nonlinear dynamics ($a \gg d$). The model time step is 7200 s, and total integration time was 20 years from spin-up. The model is forced by specifying a net transport between the eastern and western

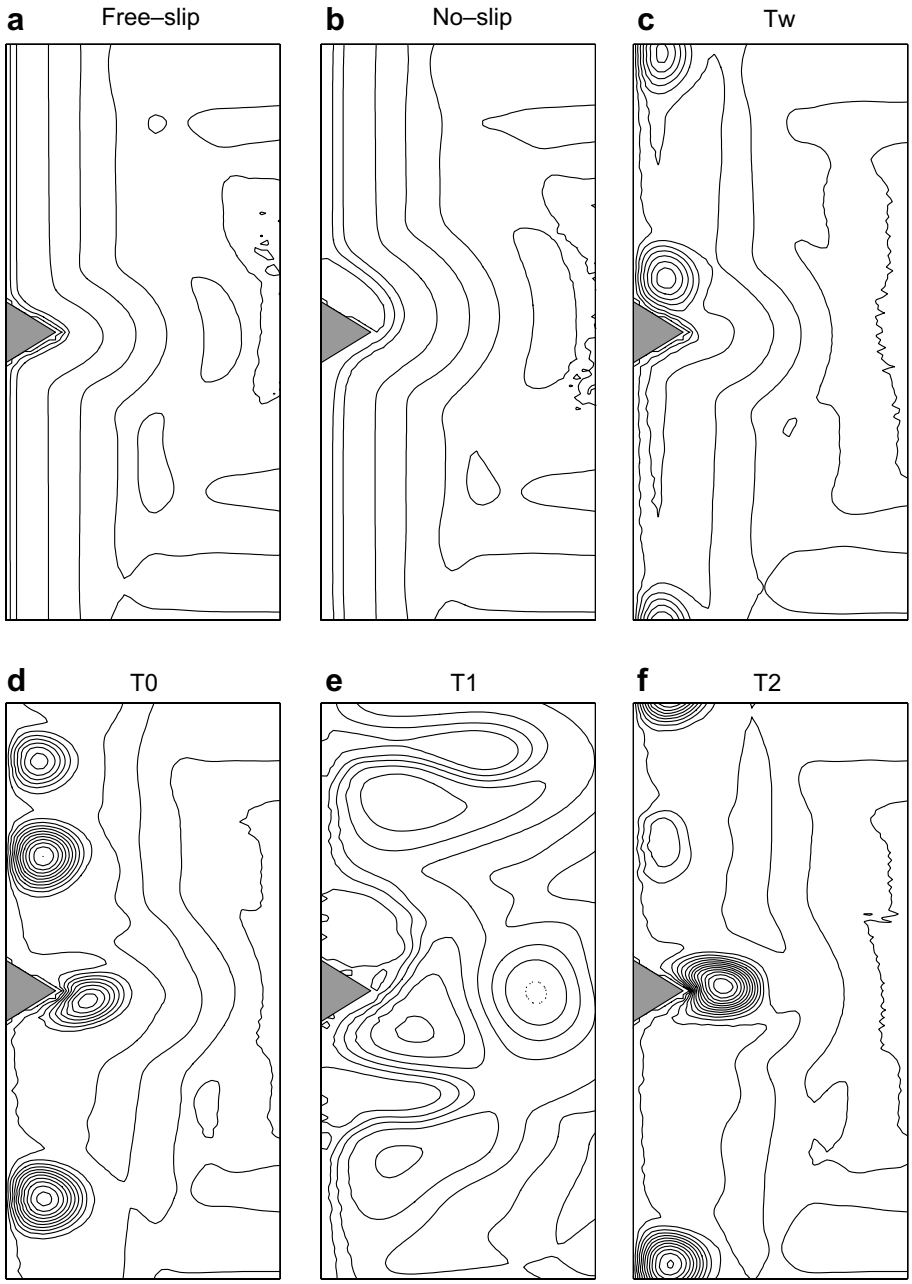

Fig. 5. Instantaneous streamlines from the QG-Cape experiment. Only the western 900 km of the model domain is shown to display the boundary current better. The contour interval is 0.5 m^2/s^2.

boundaries. There is no wind forcing $w_E = 0$. Periodic boundary conditions are used in the northern and southern boundaries, and free-slip boundary conditions are applied along the eastern boundary.

The various boundary conditions are applied additively to the potential vorticity q just before solving the Helmholtz equation (2) for ψ at each time step. The free-slip condition implies null relative vorticity so that no change is needed on q. For the no-slip condition, the second-order numerical scheme of Woods (1954, see also Verron and Blayo, 1996) is used as

$$q[i_b, j] = \frac{3(\phi[i_b + 1, j] - \phi[i_b, j])}{\Delta x} - \frac{q[i_b + 1, j]}{2}, \tag{3}$$

Table 2
Parameters of the circulation models

	QG-Cape	QG-Gyre	SWE-Gyre
$L_x \times L_y$ (km)	2000 × 3000	3000 × 3000	3000 × 3000
Δx, Δy (km)	20, 20	10, 10	20, 20
Δt (min)	120	15	20
f_0 (10^{-5} s^{-1}), β (10^{-11} s^{-1}/m)	9.34, 1.75	6.14, 2.07	9.30, 2.00
H (m), R_d (km)	500, 24	1000, 51	1000, 48
T_0 (Sv)	30	–	–
ν (m^2/s)	400	400	400–800

where $[i,j] = [x/\Delta x, y/\Delta y]$ are horizontal grid indices (with the origin at the southwest corner of the domain) and i_b is the zonal grid point of the western-boundary (western most point along each latitude).

The stochastic boundary conditions $\tilde{\zeta}[j,k]$, where $k = t/\Delta t$ is time index, are generated sequentially in time (i.e., "on line") by allocating small amount of memory for their recent past history as required by each of the Type T (regression in time) and A (translation along shore) formulations. The result is applied to the QG dynamics as

$$q[i_b, j] = q[i_b, j] + \frac{1}{a}\tilde{\zeta}[j,k] \tag{4}$$

before solving (2) at each time step k. The regression coefficients used here for the Type T SBC are given in Table 1.

4.2. The QG double-gyre (QG-Gyre) experiment

The second circulation model considered here is a wind-forced double-gyre over a 3000 km × 3000 km domain with 10 km grid spacing and 15 min time step (see Table 2). The reduced-gravity QG dynamics as Eqs. (1) and (2) is used, except that a wind forcing via Ekman pumping of the form

$$w_E(x,y) = -(1 - \lambda y/\Delta y) \times \sin(2\pi y/L_y) \tag{5}$$

is applied to the surface and that the north and south boundaries are solid walls where, along with the east boundary, the free-slip condition is applied. The constant $\lambda = 0.1$ in the forcing function (5) introduces slight asymmetry about the center latitude line to promote development of non-static steady-state flow.

The implementation strategies for the lateral boundary conditions are identical to those in the QG-Cape experiment: all lateral boundary conditions are free-slip, except along the entire length of the western boundary where the stochastic and no-slip conditions are also tested as individual cases using formulas (3) and (4).

4.3. The shallow-water double-gyre (SWE-Gyre) experiment

The third circulation experiment is also a wind-driven double-gyre simulation, except that a reduced-gravity shallow-water equation (SWE) model is used. The model domain is 3000 km × 3000 km with 20 km grid spacing, and time step is 20 min (Table 2). Our SWE model is based on the Miami Isopycnal Coordinate Ocean Model (MICOM, Bleck and Smith, 1990) whose governing equations used here are

$$\frac{\partial u}{\partial t} + \frac{\partial}{\partial x}\frac{|\vec{v}|^2}{2} - (\zeta + f)v = -g'\frac{\partial h}{\partial x} + \frac{1}{h}[\tau_x + \nabla\cdot(\nu h \nabla u)], \tag{6}$$

$$\frac{\partial v}{\partial t} + \frac{\partial}{\partial y}\frac{|\vec{v}|^2}{2} + (\zeta + f)u = -g'\frac{\partial h}{\partial y} + \frac{1}{h}[\tau_y + \nabla\cdot(\nu h \nabla v)], \tag{7}$$

$$\frac{\partial h}{\partial t} + \frac{\partial}{\partial x}(hu) + \frac{\partial}{\partial y}(hv) = 0, \tag{8}$$

where h is the layer thickness (sum of H and sea surface height), $|\vec{v}|^2 \equiv u^2 + v^2$, ζ is the relative vorticity (as before), and $g' = 0.002g$, where g is the gravity acceleration constant. The wind-stress forcing (τ_x, τ_y) is given as $\tau_y = 0$ and

$$\tau_x(x,y) = -\tau_m \cos(2\pi y/L_y) \tag{9}$$

where the constant $\tau_m = 10^{-4}\ \mathrm{m^2/s^2}$. While the windstress is symmetric about the mid-latitude, variation in the layer thickness h introduces asymmetry in the forcing term of (6) and (7) as the height difference between subtropical and subpolar gyres develops (Chassignet and Gent, 1991).

Once again, the free-slip condition governs all lateral boundaries, except along the western wall. To implement the no-slip condition and SBC formulations, an extra, fictitious line of meridional velocity array $v[i_b - 1, j]$ is created one grid-spacing Δx to the west (over the land) of the western boundary current $v[i_b, j]$, where the grid indexing $[i,j]$ and the index for the western boundary grid point i_b are as before. This fictitiously extended array of $v[i,j]$ influences the dynamics through the computation of ζ in (6) and (7) and ∇v in (7) at the western boundary. The no-slip condition is then implemented using the new line of velocity grid as $v[i_b - 1, j] = 0$, while the SBC is implemented as

$$v[i_b - 1, j] = v[i_b, j] + \tilde{\zeta}[j,k]\delta_x, \tag{10}$$

where $\tilde{\zeta}[j,k]$ is, as before, randomly generated using one of the SBC formulations and $\delta_x = 5$ km is the width of shear zone (Section 2.2). The cross-shore (u) component of the boundary current is unaffected by the SBC.

5. Results

All the SBC processes presented here are inherently zero-mean. When averaged over space and time, they are similar to the free-slip condition which prescribes zero boundary shear (and hence vorticity). Instantaneously and locally, however, the SBC vorticity values are almost always non-zero. Also, unlike the no-slip condition which affects the circulation only dissipatively, all SBC processes inject both positive and negative vorticity values into the circulation.

The circulation models, equipped with each of the boundary conditions under study, are spun-up from the rest to a dynamical steady-state. The circulation patterns at steady-state are then compared among the boundary conditions used. Diagnostic quantities such as the time-averaged mean flow field $(\bar{u}(x,y), \bar{v}(x,y))$, mean kinetic energy (MKE) $\langle u^2 + v^2 \rangle$ where the angular brackets denote space–time averaging, and eddy kinetic energy (EKE) $\langle (u - \bar{u})^2 + (v - \bar{v})^2 \rangle$ are used for the comparison. Other diagnostic quantifications specific to each model are performed as detailed later.

5.1. The QG-Cape experiment

The triangular Cape has been introduced to promote separation of the western boundary current into the domain interior at its apex. The effect of boundary conditions on such a "separation" problem is a well-studied subject (e.g., Özgökmen et al., 1997 and references therein). When a no-slip boundary condition is used, a viscous boundary layer with vorticity that dissipates energy from the interior flow is generated and advected along the boundary, thereby providing favorable conditions for a separation of the western boundary current from the coastline. Free-slip boundary conditions, on the other hand, do not generate such a viscous sublayer, so that the current tends to follow the coastline. Our runs of the QG-Cape model confirm these: the boundary current is stronger and attached along the coast for the free-slip case, while it is more dissipated and separates at the Cape for the no-slip case, in both instantaneous flow fields (Fig. 5a and b) and the mean flow fields (Fig. 6a and b).

5.1.1. Time-regression cases: "Type T" SBC

Among the SBC formulations based on temporal regression, all but the T1 case have resulted in nearly periodic sequence of strong cyclonic (dissipative) eddies that advect northward attached along the coast (Fig. 5c, d

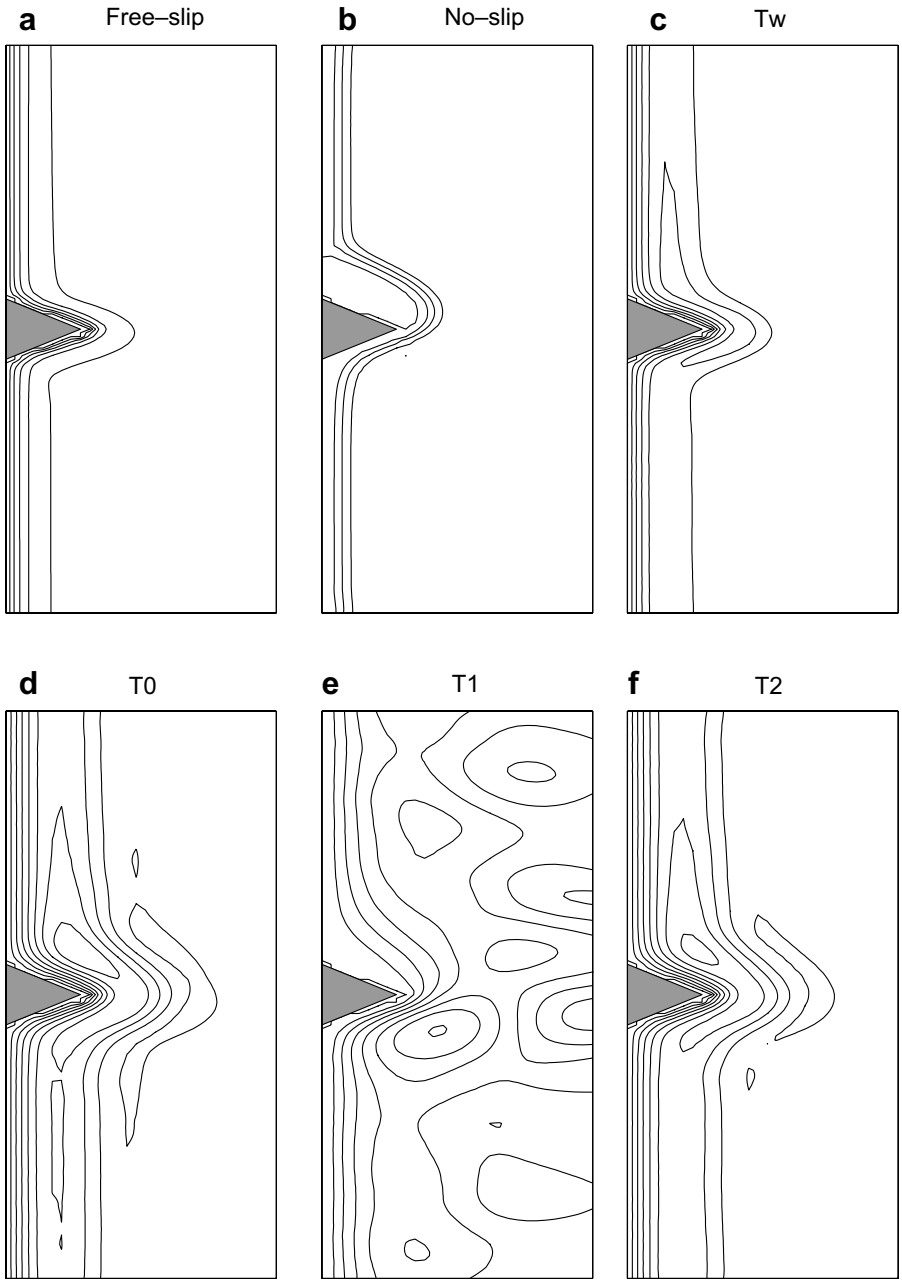

Fig. 6. Mean streamlines from the QG-Cape experiment. Only the western 600 km of the model domain is shown to display the boundary current better. Contour interval is 0.3 m^2/s^2.

and f). These advecting eddies share some qualitative features with the spin-off eddies, although their dimension relative to the boundary current width would be too large with respect to the actual ocean phenomenon. This is expected because of the lack of vertical stratification in the QG-Cape model. Similar train of eddies can also be generated when a no-slip condition is applied to a stronger flow (larger T_0 or smaller v, Berloff and McWilliams, 1999). For these SBC cases (Tw, T0, T2), however, the boundary current does not separate from the coast, as observed from their mean flow fields (Fig. 6c, d and f). The lone exception is T1, the long time-constant SBC model, where the train of eddies is replaced by a meandering boundary current (Fig. 5e) and the mean boundary current separates from the coast at the Cape (Fig. 6e). The mean

flow fields of Fig. 6 also indicate that, among all the Type T SBC as well as free-slip and no-slip cases, only T1 has produced circulation features which consistently penetrate into the interior domain (towards east). This implies that the T1 boundary condition has a potential for controlling the horizontal mixing at meso-scale in numerical simulations.

Table 3 lists MKE and EKE values from the QG-Cape experiments. The T1 and no-slip cases have relatively similar MKE values, while all other Type T SBC cases have much higher MKE similar to the free-slip cases. The lower MKE in the T1 and no-slip cases is consistent with the formation of the dissipative boundary layer that helps the current to separate from the coast. On the other hand, the eddy diagnostics indicate that the no-slip and free-slip cases with near-zero EKE are static and the Type T SBC cases with the substantially larger EKE values are turbulent. This underscores that separation of the boundary current from the coast is a episodic event in the T1 case, while it is a permanent feature in the no-slip case. To quantify the "separation", we have recorded the cross-shore distance between the coast and boundary current (as determined by the location of the maximum v speed) at the downstream (northern) base of the Cape. This separation distance confirms the episodic nature of the T1 flow field (Fig. 7 and Table 3).

Clearly, the T1 boundary condition influences the mean flow features more than other Type T SBC formulations as well as the traditional free-slip and no-slip. The T1 formulation is derived from the low-frequency behaviors of the observation data $\tilde{\zeta}$. This low-frequency end of the power spectrum is generally under-estimated by our regression fit for the Type T models other than T1 (Fig. 4), including for the T0 model with 50 regression coefficients. This indicates that the low-frequency signals, with time-scales on the order of several days to a week, are crucial for parameterization of the boundary layer dynamics.

The results presented here, especially the uniqueness of T1 over other formulations, are confirmed qualitatively when the experiment is repeated with a shorter model time step of $\Delta t = 1$ h.

5.1.2. Advection cases: "Type A" SBC

For the Type A SBC formulation, we have tested with along-shore advection velocities of 60, 10, 1, and 0 cm/s. The advection speed of 60 cm/s is consistent with the OSCR data. The A(60) case displays substantial meso-scale activity with a modest amount of mean separation distance (Fig. 8a). The separation distance, however, varies more widely and rapidly for the A(60) case than T1 (Fig. 7 and Table 3). As the advection speed parameter is decreased, the separation becomes more pronounced (Fig. 8b–d). In particular, the A(0) boundary condition is spatially random yet temporally invariant, and its effects on the flow field are quite similar to those of no-slip, especially in terms of separation of the mean boundary current. The similarities between the Type A and no-slip cases have eroded quickly as non-zero advection speed is introduced. In particular, the A(1) case, representing only a slight increase in the advection speed to 1 cm/s, is substantially more turbulent and separation is more episodic, as indicated by the EKE value and standard deviation of the separation index.

We note again that the Tw scheme is equivalent with A(∞). Table 3 indicates that a variety of the mean flow diagnostic quantities can be controlled just by adjusting the advection speed parameter of the Type A SBC, which models $\tilde{\zeta}$ as a white noise advected along shore. The separation diagnostic is larger and more

Table 3
The mean kinetic energy (MKE), eddy kinetic energy (EKE), and the separation index (distance from the shore to the boundary current at the upstream base of the Cape, shown with the standard deviation value) from the simulations in the QG-Cape experiment

BC	MKE (cm^2/s^2)	EKE (cm^2/s^2)	Separation (km)
Free-slip	62.5508	0.0001	40.0 ± 0.0
No-slip	24.1350	0.0001	240.0 ± 0.0
Tw	66.4904	33.6006	47.5 ± 18.4
T0	76.6429	146.8851	77.4 ± 56.9
T1	27.9508	101.8551	288.2 ± 177.8
T2	74.7997	138.5754	72.1 ± 42.0
A(60)	42.0666	184.7789	169.0 ± 203.0
A(10)	19.0791	27.8941	182.0 ± 143.0
A(1)	11.7133	29.4561	185.1 ± 102.0
A(0)	25.5252	0.3662	240.0 ± 0.0

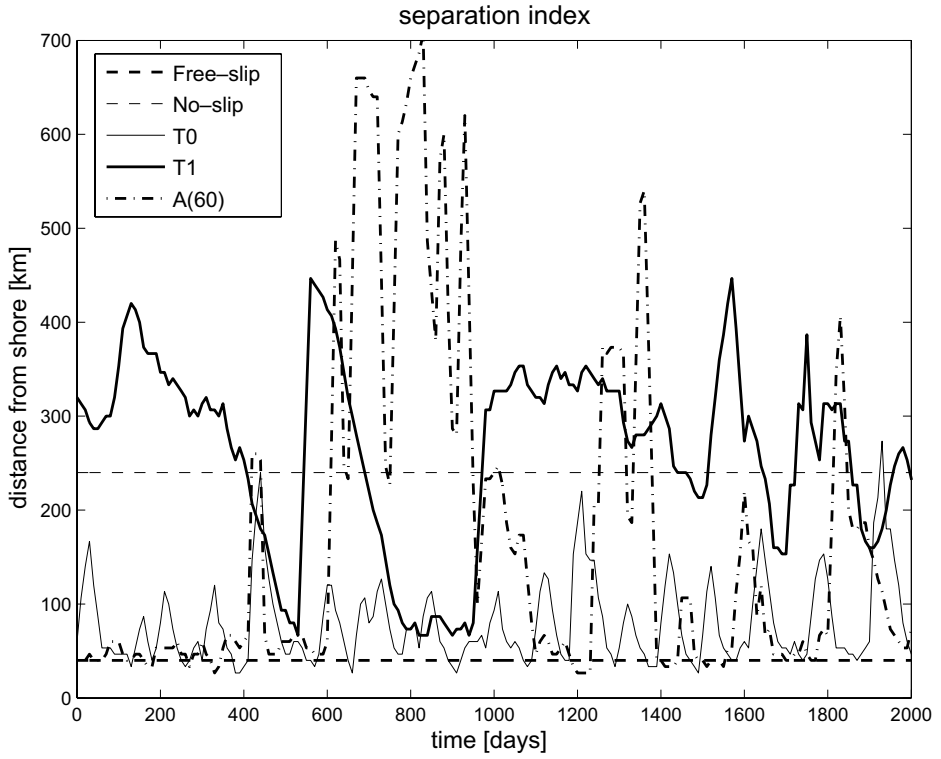

Fig. 7. The distance between the shore and the location of maximum current ("separation index") measured at the latitude of the northern base of the Cape.

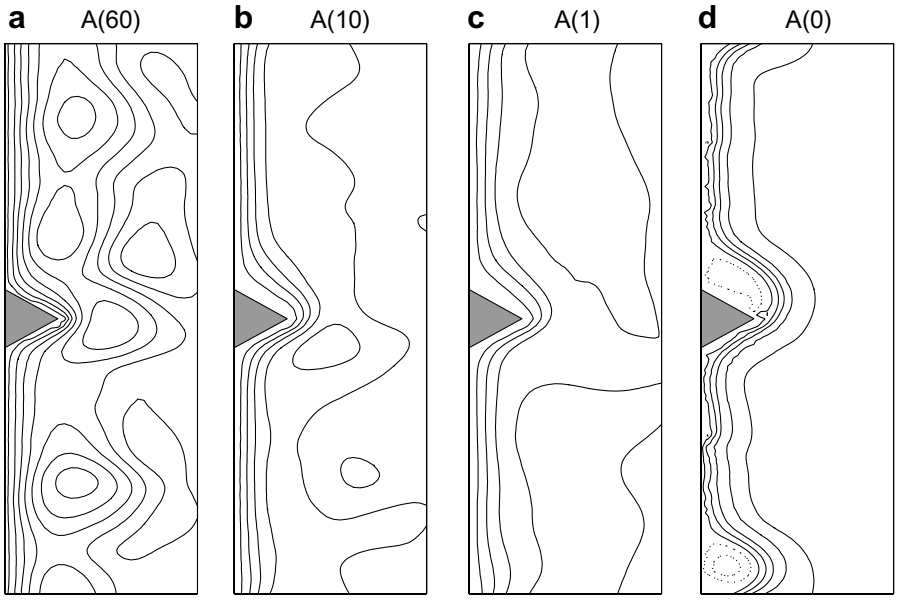

Fig. 8. The same as Fig. 6, except that mean streamlines from the Type A cases are shown.

stable (smaller standard deviation) when the advection speed is smaller. A substantial meso-scale behavior is recognized in the mean flow only in the A(60) case, that is based on the OSCR empirical parameters, and not

on other Type A cases including Tw. The A(60) SBC achieves this by introducing zero-mean boundary vorticity (dissipation) while the no-slip formulation is constantly dissipative.

Numerical implementation of the Type A SBC may be an issue. Differential advection scheme cannot be applied directly to coastal grid points due to the CFL limitation and high-wavenumber contents of the white noise process being advected. We have used an interpolation to smooth the SBC signal to facilitate realization of advection. These numerical manipulations can introduce errors, and the overall similarities in the results of the A(10) and A(1) cases may be attributed, at least partially, to such errors in realization. A more serious difficulty is variation in advection speed. The assumption that the advection is constant along-shore may be acceptable for a channel configuration like the QG-Cape model but is unrealistic even in an idealized double-gyre configuration where along-shore advection changes both in magnitude and sign. In summary, a more sophisticated numerical scheme is required to realize the Type A and similar SBC schemes that use the along-shore advection as a parameter.

5.1.3. *Effects of viscosity*

To examine if the performance of SBCs as presented above is affected strongly by circulation model's horizontal viscosity ν, we have repeated the no-slip and T1 cases using values ranging $\nu = 200$–800. As expected, the flow becomes more turbulent for the low viscosity cases, as reflected by increases in the EKE (Fig. 9) and variability in the separation distance (Table 4) as the viscosity is lowered. The rates of increase for the T1 cases are higher than no-slip cases. The mean flow features such as MKE and mean separation distance, however, remain relatively constant over the range of ν. implying a stable performance of T1. The T1 cases have also remained turbulent (no-zero EKE) over the entire range of ν, while the flows from the no-slip cases are static for $\nu \geqslant 400$. The T1 boundary condition, with appropriate parameter values, hence has a potential application to control mixing (at least over regions near western boundaries) in a climate scale OGCM where a high viscosity parameter is typically used.

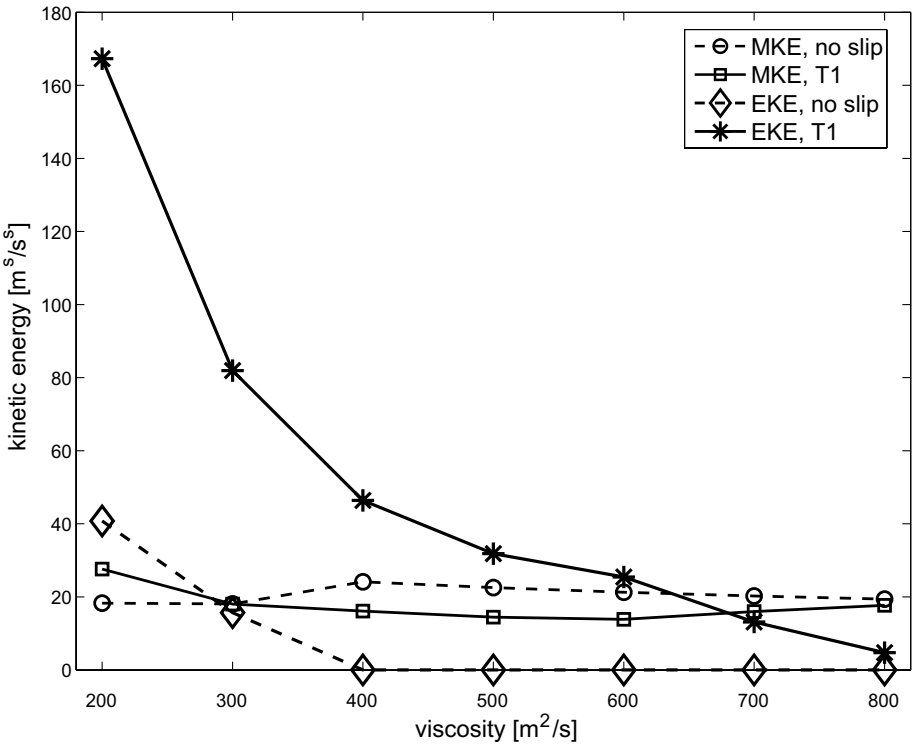

Fig. 9. Mean (MKE, thin lines) and eddy (EKE, thick lines) kinetic energy as a function of viscosity (ν) from the no-slip (dashed lines) and T1 (solid lines) cases of the QG-Cape experiment.

Table 4
The separation index (see Table 3) as a function of the viscosity parameter v in the QG-Cape experiment

v	No-slip (km)	T1 (km)
200	233.9 ± 35.0	300.8 ± 216.2
300	260.2 ± 115.4	284.7 ± 212.4
400	240.0 ± 0.0	288.2 ± 177.8
500	220.0 ± 0.0	266.5 ± 171.2
600	220.0 ± 0.0	203.4 ± 136.6
700	220.0 ± 0.0	257.1 ± 217.6
800	220.0 ± 0.0	189.1 ± 52.9

5.2. The QG-Gyre experiment

For the double-gyre experiments, only the Tw and T1 SBC formulations are used along with the free-slip and no-slip boundary conditions. The other Type T boundary conditions have been shown not as effective as T1 in affecting mean circulation features. Also, as previously discussed, the Type A formulations still have issues in numerical realization of the along-shore advection especially when the advection velocity varies over space. Further studies of the Type A cases are thus deferred for future. The Tw case is included in the present study mostly as a reference, since a white-noise process is a common component in both Type T and A formulations. The stochastic and no-slip boundary conditions are applied uniformly along the western boundary on both the subtropical and subpolar sides.

All four cases have resulted in mean flow fields with the characteristic double-gyre circulation pattern with subpolar and subtropical gyres (Fig. 10) and a strong eastward current, or the mid-latitude jet, between them.

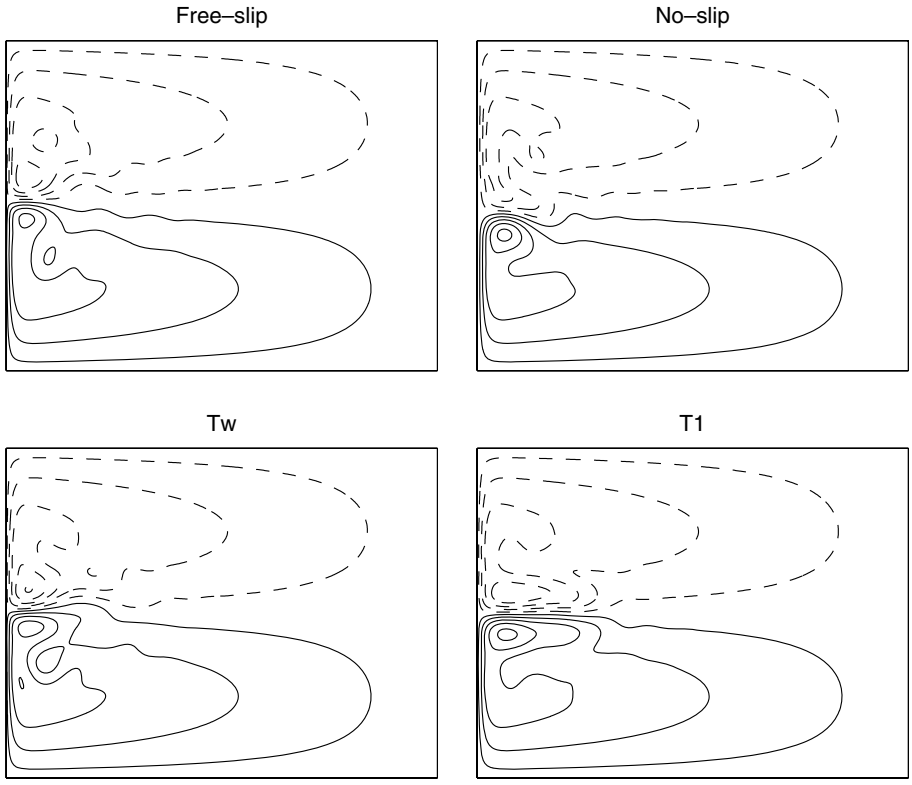

Fig. 10. Mean stream function fields from the QG-Gyre experiment. The contour interval is 0.2 m^2/s^s, with positive/negative values in solid/dashed lines.

Dynamic tendencies are, however, significantly different among these cases. In the free-slip case, the mid-latitude jet is turbulent with large-magnitude meanders that frequently close off to form cyclonic and anti-cyclonic rings almost immediately after separation from the western boundary. This behavior is due to the asymmetry prescribed in the wind forcing (Chassignet and Gent, 1991) that leads to a stronger subtropical gyre than its subpolar counterpart. The no-slip case often displays "premature separation" of the western boundary currents, where both gyres stay away from the mid-latitude and two separated boundary currents are formed, due to lateral friction (Haidvogel et al., 1991). Because of the weaker subpolar gyre, the boundary and mid-latitude currents associated with it are often too inconspicuous to be identified, and this has resulted in the more tropical location of the mid-latitude jet in the mean flow field. The Tw case is in general similar to the free-slip case, implying lack of impact by this particular SBC. The T1 case, on the other hand, displays much less turbulent mid-latitude jet and fewer rings formed than the free-slip and Tw cases, while it shows no sign of premature separation.

The phenomenological similarities between the free-slip and Tw cases are also confirmed by their MKE and EKE values (Table 5). The MKE and EKE of the T1 case are both between respective values of the free-slip and no-slip cases, confirming that the T1 flow is less turbulent than the free-slip flow and less dissipative than the no-slip flow.

The mid-latitude jet in the T1 case has penetrated, on average, more deeply into the basin interior than the other three cases (Fig. 10). A plot of the maximum zonal speed as a function longitude (Fig. 11) indicates that the jet from the T1 case decays to half of its maximum magnitude after penetrating almost twice as far into the basin interior (approximately 650 km) as other cases (250–350 km). The maximum speed of the mean jet tends to be larger for the two SBC cases than the free-slip and no-slip cases. In the free-slip (and Tw) case, stable mid-latitude jet tends not to persist due to the turbulent flow caused by the asymmetric forcing, which makes the subtropical gyre deeper than the subpolar gyre. As a consequence, the pole-ward western boundary current is stronger than its equator-ward counterpart, and the location where the jet separates the coast tends to overshoot pole-ward. The mean jet-separation latitude (Table 6, first column) confirms this pole-ward bias for the free-slip and Tw cases. For the no-slip case, the mean separation latitude has moved drastically equator-ward due to effect of the premature separation described previously. For the T1 case, the jet separates very close to the latitude along which the wind forcing has zero wind-stress curl. Relative robustness and longevity of the T1 mid-latitude jet can then be explained by its location where the neighboring two gyres are relatively free of conflict against the forcing in terms of the sign of vorticity. It is not certain that the T1 SBC can inherently place the jet in such a favorable location, although T1 does move the separation point in the *direction toward* such an optimum. Still, this experiment demonstrates that SBCs can impact the outcome of OGCM simulations with respect to prominent flow features in a way that neither free-slip and no-slip can.

5.3. The SWE-Gyre experiment

The SWE dynamics have more degrees of freedom than QG counterparts. As detailed previously, the SBC perturbs only the along-shore component of the boundary velocity, while the cross-shore component and the material (h) field are unaffected.

The double-gyre experiment is repeated with the SWE circulation model using three different viscosity values $\nu = 400$, 600, 800 m^2/s. This time, all four boundary condition cases of free-slip, no-slip, Tw, and T1 have maintained the characteristic double-gyre flow fields throughout the stead-state for each value of ν,

Table 5
The mean kinetic energy (MKE) and eddy kinetic energy (EKE) from the QG-Gyre experiment

BC	MKE	EKE
Free-slip	210.4	143.5
No-slip	81.1	32.2
Tw	213.9	134.5
T1	157.7	74.4

The unit is cm^2/s^2.

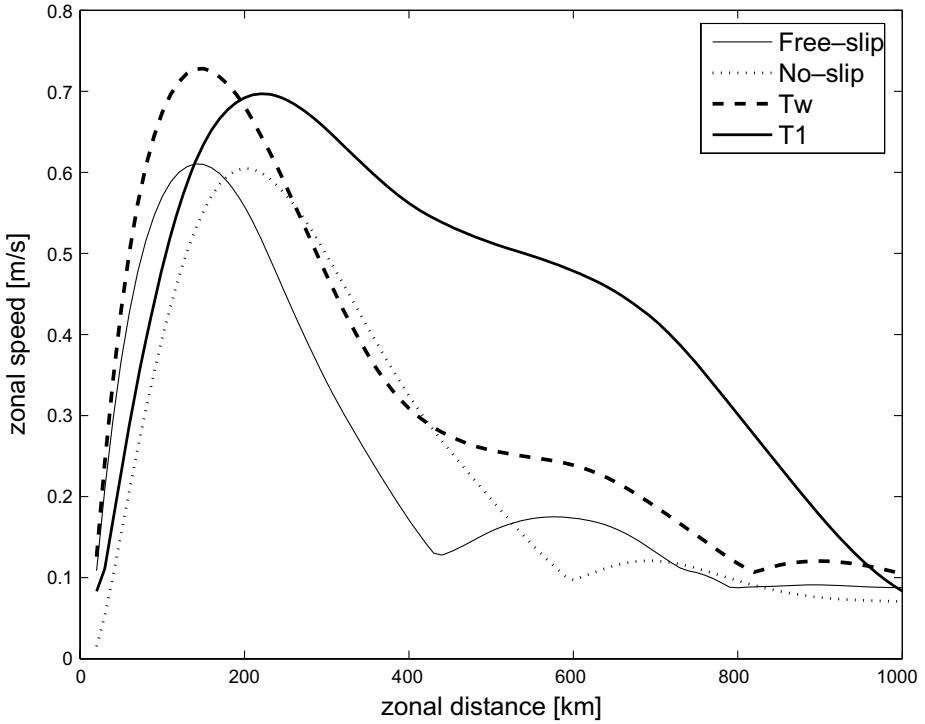

Fig. 11. The maximum speed of zonal current as a function of longitude (zonal distance from the western boundary) in the QG-Gyre experiment.

Table 6
The jet separation latitude, measured by the distance (km) from the zero wind-stress curl line (ZWCL), in the double-gyre experiments

BC	QG-Gyre	SWE-Gyre		
	$v = 400$	$v = 400$	$v = 600$	$v = 800$
Free-slip	42.6 ± 81.5	-60.9 ± 99.9	-70.5 ± 61.0	-54.4 ± 01.0
No-slip	-77.4 ± 59.9	-18.3 ± 17.4	-50.3 ± 07.2	-13.3 ± 18.7
Tw	24.4 ± 85.5	-76.9 ± 58.8	-62.6 ± 67.8	-54.4 ± 01.2
T1	-0.7 ± 71.0	-83.2 ± 78.6	-87.4 ± 55.3	-65.2 ± 53.1

Positive values thus indicate pole-ward deviation from ZWCL, and negative equator-ward. The temporal mean as well as the corresponding standard deviation values are shown.

and differences among them are more subtle than in the QG-Gyre experiment. For example, the mid-latitude jet is well-developed in each case, and the T1 case shows no particular advantage in regards to jet penetration. The jet separation latitude for the T1 case is, however, the furtherest to the south (equator-ward) among all boundary conditions, for each value of v (Table 6). The other boundary condition cases also result in equator-ward overshooting but not as extensively as the T1 case. In the MICOM numerics used in our SWE, the wind-induced acceleration depends on the layer-thickness, stronger in the cyclonic subpolar gyre (shallower h) and weaker in the anti-cyclonic subtropic gyre (deeper h). As a consequence, the equator-ward overshooting of the mid-latitude jet can be interpreted as an indication that, when integrated over the model domain, the T1 flow field has the most strongly developed set of two gyres.

The T1 boundary condition is the only case which stayed energetic in the meso- and finer scales for each value of v. In contrast, all other boundary conditions have produced steady-state flow fields which are practically static. For example, for the most viscous configuration ($v = 800$), only T1 case is able to generate rings off the mid-latitude jet (and have done so consistently). The energy diagnostics (Table 7) confirms this numerically. Specifically, all but T1 cases have EKE values lower than 10 for some values of v. These observations

Table 7
Mean kinetic energy (MKE) and eddy kinetic energy (EKE) from the SWE-Gyre experiments

BC	MKE			EKE		
	$\nu = 400$	$\nu = 600$	$\nu = 800$	$\nu = 400$	$\nu = 600$	$\nu = 800$
Free-slip	90.1	56.4	66.0	259.7	129.9	2.2
No-slip	87.8	35.5	25.3	39.1	3.9	11.7
Tw	84.6	65.2	66.0	246.0	143.1	1.2
T1	69.5	48.3	38.2	211.6	117.3	66.3

indicate that the T1 SBC can enhance kinetic activities over a broad range of circulation and turbulence scales and that it is more effective in doing so than other boundary conditions tested here, especially for a high viscosity model typical for climate simulations.

6. Concluding remarks

State trajectory of an OGCM is known to be sensitive to initial conditions, forcings, and boundary conditions. It is then not surprising that different SBCs lead to significantly different circulation patterns. Since fluid flows are chaotic with respect to the boundary conditions as well as initial conditions, it is important to accurately model the sub-grid scale processes in the boundary layer. Some of the SBCs examined here have indeed perturbed the basin-wide flow for a circulation model dominated by geostrophic turbulence, where the high-wavenumber vorticity anomaly induced by SBCs has caused significant low-wavenumber variability in the whole domain. The changes in circulation pattern have taken place even though these SBCs have zero long-term mean.

We have demonstrated that the T1 boundary condition, based on a simple order-1 auto-regression stochastic process, is capable of controlling the basin-scale circulation patterns and energetics in ways that are significantly different from the traditional free-slip and no-slip conditions. The new boundary condition is particularly attractive for climatic time-scale ocean modeling due to its ability in maintaining higher level of eddy-scale activities than both free-slip and no-slip under a highly viscous (e.g., $\nu = 800\ \mathrm{m^2/s}$) operating condition. Phenomenologically, the T1 formulation applied to the western boundary has promoted separation of the boundary current and strengthening of the mid-latitude jet, without sacrificing as much eddy-scale energy as the common no-slip formulations.

Dynamical properties of the SBCs may be understood in more details through simulations using finer resolution circulation models than ones presented here. For example, Lee (2001) has shown that the western boundary current in a barotropic QG model can be split into two zones: a viscous sublayer very close to the wall, in which viscous dissipation actually takes place, and an inertial shear layer which serves as an interface of shear production and exchange of Reynolds stresses between the viscous sublayer and outer flows. When the lateral viscosity is very high as in coarse resolution models, the viscous layer expands over the inertial layer, and Reynolds stresses are suppressed. An effect of our SBC formulation is to restore such under-resolved Reynolds stresses through a boundary condition. A key question is then how the vorticity anomaly supplied as a boundary condition can propagate across the two viscous sublayers and affect Reynolds stresses in the outer layer. Also, another remaining question is how the SBCs perform in baroclinic models, which require formulation of boundary conditions for the subsurface layers that our data in hand do not indicate directly. The experiments presented here do indicate, however, that high-frequency (approximately daily and higher) components of an SBC tend to disrupt formation of viscous sublayer that facilitates coast-separation and interior-penetration of the western boundary current. Persistency is thus a key attribute of an effective SBC.

The T1 regression formula has two numerical parameters: the correlation time-scale τ_1 and forcing strength $\sigma^2\Delta t$, where σ^2 is the variance parameter for a random number generator and Δt is the model time step (which ranged from 15 min to 2 h in our experiments). We have used the OSCR High-Frequency (HF) radar measurements to estimate these parameters to be $\tau_1 \approx 7$ days and $\sigma^2\Delta t \approx 2.6 \times 10^{-10}\ \mathrm{s^{-1}}$. Since any OGCM configuration has a unique resolution characteristics, it is likely that these parameter values need to be adjusted for

each application. In the experiments presented here, however, we simply used the OSCR observation-based parameter values for the three different models used, and simulations using a more optimized set of the parameter values as well as optimization of the parameters themselves are deferred for the future. Uncertainty about the relationships between the parameters and large-scale flow pattern is an outstanding issue in stochastic parameterization approaches in general.

By comparison of several different regression formulations, we find that the relatively long correlation time-scale τ_1 to be the critical component of the T1 boundary condition. In a recent work on random sub-grid scale forcing, Berloff (2005) has reported that the western boundary is a key region to determine and apply the stochastic forcing to induce eddy activities and that an effective correlation time-scale for the stochastic forcing is approximately 3 days. We have repeated some of the experiments using τ_1 values of 3–21 days and observed similar flow characteristics as the 7-day cases presented here, although the observed T1 characteristics such as separation of boundary current in QG-Cape model tend to erode as τ_1 is decreased. We thus conclude that our results are in general agreement with the above observations by Berloff (2005), who has also noted eastward extension of the mid-latitude jet as we have observed in the QG-Gyre experiment.

Several simplifying approximations on the observed data have been made to facilitate the stochastic formulations. For example, in all Type T formulations, we have neglected the spatial correlation in $\tilde{\zeta}(y,t)$ since the observed correlation scale is approximately at the lowest end of our target grid spacing of 10 km and larger. Also, the observed mean vorticity $\hat{\zeta}_m$ has been neglected in our studies to focus on the vorticity variabilities. The mean, annual harmonics, and other deterministic components can certainly be added to SBCs; the effects of these enhanced SBCs on the circulation would then have to be re-examined due to nonlinearity. Finally, the T1 boundary condition is derived from the HF data by removing the 10-h periodicity, an integral component in our preliminary SBC formula (Mariano et al., 2003), since Soloviev et al. (2003) have brought to our attention about seasonal dependency of this prominent high-frequency periodicity. Such design decisions can be made more exactly with the use of more recent HF observation data sets with more extensive coverage in space and time. A longer along-shore coverage would be especially beneficial in refinement of our boundary models in terms of their wavenumber contents, and a better understanding of high-wavenumber components may lead to a more practical formulation for the advection procedure in the Type A formulations. Such observation data are becoming available along the US coasts among other areas, and the use of them is another topic of future study.

Acknowledgement

This work was supported by the National Science Foundation, US, OCE-0136700. The authors wish to thank Prof. L.K. Shay for collaborations on the OSCR surface current data.

References

Beckman, A., Böning, C.W., Köberle, C., Willebrand, J., 1994. Effects of increased horizontal resolution in a simulation of the North Atlantic Ocean. J. Phys. Oceanogr. 24, 326–344.

Berloff, P.S., 2005. Random-forcing model of the mesoscale oceanic eddies. J. Fluid Mech. 529, 71–95.

Berloff, P., McWilliams, J., 1999. Quasigeostrophic dynamics of the western boundary current. J. Phys. Oceanogr. 29, 2607–2633.

Bleck, R., Smith, L.T., 1990. A wind-driven isopycnic coordinate model of the north and equatorial Atlantic ocean 1. Model development and supporting experiments. J. Geophys. Res. 95, 3273–3285.

Böning, C., 1986. On the influence of frictional parameterization in wind-driven circulation models. Dyn. Atmos. Ocean 10, 63–92.

Böning, C.W., Bryan, F.O., Holland, W.R., 1994. Thermohaline circulation and meridional heat transport in a high resolution model of the North Atlantic Ocean. EOS Trans. 75, 63.

Chassignet, E.P., Gent, P.R., 1991. The influence of boundary conditions on midlatitude jet separation in ocean numerical models. J. Phys. Oceanogr. 21, 1290–1299.

DiGiacomo, P.M., Holt, B., 2001. Satellite observations of small coastal ocean eddies in the Southern California Bight. J. Geophys. Res. 106, 22521–22543.

Griffa, A., Castellari, S., 1991. Nonlinear general circulation of an ocean model driven by wind with a stochastic component. J. Mar. Res. 49, 53–73.

Haidvogel, D., McWilliams, J., Gent, P., 1991. Boundary current separation in a quasigeostrophic, eddy-resolving ocean circulation model. J. Phys. Oceanogr. 22, 882–902.

Leaman, K.D., Johns, E., Rossby, T., 1989. The average distribution of volume transport and potential vorticity with temperature at three sections across the Gulf Stream. J. Phys. Oceanogr. 19, 36–51.

Lee, T.N., 1975. Florida current spin-off eddies. Deep Sea Res. 22, 753–765.

Lee, S.-K., 2001. On the structure of supercritical western boundary currents. Dyn. Atmos. Ocean 33, 303–319.

Lee, T.N., Atkinson, L.P., 1983. Low-frequency current and temperature variability from Gulf Stream frontal eddies and atmospheric forcing along the southeast US outer continental shelf. J. Geophys. Res. 88, 4541–4567.

Lee, T.N., Atkinson, L.P., Legeckis, R., 1981. Observations of a Gulf Stream frontal eddy on the Georgia continental shelf, April 1977. Deep Sea Res. 28, 347–378.

Mariano, A.J., Chin, T.M., Özgökmen, T.M., 2003. Stochastic boundary conditions for coastal flow modeling. Geophys. Res. Lett. 30, 1457. doi:10.1029/2003GL01697.

Munk, W., Armi, L., Fischer, K., Zachariasen, F., 2000. Spirals on the sea. Proc. R. Soc. Lond. A 456, 1217–1280.

Özgökmen, T.M., Chassignet, E.P., Paiva, A.M., 1997. Impact of wind forcing, bottom topography, and inertia on midlatitude jet separation in a quasigeostrophic model. J. Phys. Oceanogr. 27, 2460–2476.

Peters, H., Shay, L., Mariano, A., Cook, T., 2002. Current variability on a narrow shelf with large ambient vorticity. J. Geophys. Res., 107, 10.1029/2001JC000813.

Schlichting, H., 1979. Boundary Layer Theory, seventh ed. McGraw-Hill.

Shay, L., Cook, T., Haus, B., Martinez, J., Peters, H., Mariano, A., VanLeer, J., An, P., Smith, S., Soloviev, A., Weisberg, R., Luther, M., 2000. VHF radar detects oceanic submesoscale vortex along Florida coast. EOS Trans. 81, 209–213.

Shay, L., Cook, T., Peters, H., Mariano, A., Weisberg, R., An, P., Soloviev, A., Luther, M., 2002. Very high-frequency radar mapping of surface currents. IEEE J. Oceanic Eng. 27, 155–169.

Soloviev, A., Luther, M., Weisberg, R., 2003. Energetic baroclinic super-tidal oscillations on the shelf off southeast Florida. Geophys. Res. Lett. 30, art. no. 1463.

Treguier, A.M., 1992. Kinetic energy analysis of an eddy resolving primitive equation model of the North Atlantics. J. Geophys. Res. 97, 687–701.

Treguier, A.M., Hua, B., 1987. Oceanic quasi-geostrophic turbulence forced by stochastic fluctuations. J. Phys. Oceanogr. 17, 397–411.

Verron, J., Blayo, E., 1996. The no-slip condition and the separation of western boundary currents. J. Phys. Oceanogr. 26, 1938–1951.

Woods, L.C., 1954. A note on the numerical solution of fourth order differential equations. Aeronaut. Quart. 5, 575–583.